



RESEARCH ARTICLE

WILEY

Numerical investigation on performance of three solution reconstructions at cell interface in DVM simulation of flows in all Knudsen number regimes

L.M. Yang¹ | C. Shu¹  | W.M. Yang¹ | J. Wu²  | M.Q. Zhang¹

¹Department of Mechanical Engineering,
National University of Singapore,
Singapore

²Department of Aerodynamics, College of
Aerospace Engineering, Nanjing, China

Correspondence

C. Shu, Department of Mechanical
Engineering, National University of
Singapore, 10 Kent Ridge Crescent,
Singapore 119260.
Email: mpeshuc@nus.edu.sg

Funding information

National Research Foundation Singapore;
Sembcorp Industries Ltd; National
University of Singapore; Sembcorp-NUS
Corporate Laboratory, Ministry of
Education (MOE) Singapore; National
Natural Science Foundation of China,
Grant/Award Number: 11772157

Summary

In the conventional discrete velocity method (DVM), the local solution of collisionless Boltzmann equation with a piecewise constant distribution for the distribution function is utilized to reconstruct distribution function at the cell interface and then calculate numerical flux of Boltzmann equation for updating the distribution function at cell center. In this process, a numerical dissipation will be introduced into the solution due to neglecting of the collision effect at the cell interface. This numerical dissipation may deteriorate the solution accuracy of conventional DVM in the continuum flow regime, in which the particle collision happens frequently. To overcome this defect, two improved schemes are first presented in this work, in which the local discrete solution of Boltzmann equation with Shakhov model is adopted to evaluate the distribution function at the cell interface, while the equilibrium state of the local solution is computed by different ways. One of the improved schemes evaluates the equilibrium state exactly by the moments of distribution functions according to the compatibility condition, while the other computes the equilibrium state approximately by a simple average at the cell interface. Since the collision effect is incorporated in evaluation of numerical flux, the improved schemes can provide reasonable solutions in all flow regimes. On the other hand, they introduce some extra computational efforts for determining the collision term at the cell interface as compared with the conventional DVM. To assess the performance of different methods for simulation of flows in all flow regimes, a comprehensive study is then carried out in this work.

KEYWORDS

all flow regimes, computational efficiency, discrete velocity method, solution accuracy, solution reconstruction

1 | INTRODUCTION

The discrete velocity method (DVM) or discrete ordinate method (DOM) has been widely used to solve rarefied flow problems in recent years.^{1–10} Its applications include the field of spacecraft and re-entry vehicle,^{11,12} microelectromechanical system,^{13,14} plasma transport,^{15,16} and phonon heat transfer and multiple frequency radiative transport.^{17–20} The DVM is to

resolve the Boltzmann equation in both the physical space and particle velocity space. After discretization in the particle velocity space, a set of partial differential equations, which is generally called the discrete velocity Boltzmann equation (DVBE), is obtained. For ease of solving flow problems with curved boundary, the finite volume method (FVM) is commonly adopted to discretize the DVBE in the physical space. Furthermore, to update the discrete distribution function at cell center, the numerical flux at the cell interface has to be determined in advance, which is equivalent to reconstruct the distribution function at the cell interface from those at cell centers of two neighboring cells. The way of solution reconstruction at the cell interface has a significant effect on the performance of DVM in different flow regimes, which will be investigated comprehensively in this work.

In the conventional DVM, the distribution function at the cell interface is evaluated by upwind scheme directly, such as the second-order scheme with slope limiter function,^{21,22} third-order upwind scheme,²³ essentially non-oscillatory scheme,²⁴ and weighted essentially non-oscillatory scheme.^{25,26} Taking the second-order scheme with slope limiter function as an example. An initial piecewise constant distribution, which is constructed by the second-order scheme with slope limiter function, is first assumed for the distribution functions at the left and right sides of cell interface.²² The numerical flux at the cell interface is then computed by multiplying the initial distribution function with the discrete particle velocity according to the direction of particle velocity. With this way, the evolution of distribution functions at cell centers is independent of each other at each time level. As a result, the computation of the conventional DVM is relatively simple and efficient. On the other hand, it should be indicated that this process is equivalent to reconstructing the local solution by solving collisionless Boltzmann equation, in which the collision effect at the cell interface is ignored.^{27,28} As compared to the solution of Boltzmann equation with collision term, the collisionless solution will introduce a numerical dissipation that is proportional to the mesh size.²⁹ This numerical dissipation may deteriorate the solution accuracy of conventional DVM in the continuum flow regime, in which the particle collision happens frequently and the physical viscosity is relatively small. To get reasonable solutions, the conventional DVM usually requires to use very small cell size in comparison with the mean free path as commented by Xu and Liu.²⁹

Within the framework of DVM, the unified gas kinetic scheme (UGKS)³⁰⁻³³ and the discrete unified gas kinetic scheme (DUGKS)³⁴⁻³⁷ have been developed to overcome the defect of poor accuracy of the conventional DVM in the continuum flow regime. Different from the conventional DVM, both UGKS and DUGKS calculate the distribution function at cell interface by the local solution of Boltzmann equation with collision term. Specifically, UGKS adopts the local integral solution of DVBE to reconstruct the distribution function at the cell interface, while DUGKS evaluates this distribution function from the local characteristic solution of DVBE. In the calculation of the local solution of DVBE, both the particle transport and collision processes are considered, and the piecewise linear distribution for the distribution function is assumed at the cell interface. Owing to the fact that the collision effect is considered in the solution reconstruction at cell interface, both UGKS and DUGKS can provide good predictions of flow prosperities in all flow regimes. However, in these two methods, the equilibrium distribution function at the cell interface has to be calculated for determining the collision term. Moreover, a large number of coefficients related to the conservative variables and their derivatives are required for calculating the local integral solution of DVBE in UGKS, and in DUGKS, several transformations are needed for updating the distribution function. These extra manipulations lead the UGKS and DUGKS to be more complicated than the conventional DVM. Accordingly, more computational efforts are required by these two methods.

From the above discussions, it is found that the physical reconstruction of the local solution with collision effect at the cell interface is the key to improve the solution accuracy of conventional DVM in the continuum flow regime. Given this realization, two improved methods for solution reconstruction at the cell interface are presented in this work. In the developed schemes, the local characteristic solution of DVBE with Shakhov model is utilized to compute the distribution function at the cell interface. For ease of implementation, the first-order implicit scheme is used to discretize the collision term in deriving the local solution of DVBE. By this way, the local solution can be expressed as a linear combination of the distribution function at the surrounding points of cell interface and the equilibrium state on the cell interface. The distribution function at the surrounding points of cell interface is computed by the initial piecewise linear distribution for the distribution function. For calculation of the equilibrium state on the cell interface, the conservative variables and heat flux at the same physical location have to be determined in advance. In the first improved scheme, these flow variables are calculated by the distribution function at the surrounding points of cell interface according to the compatibility condition. In this process, the moments of distribution function in the whole particle velocity space need to be computed. To reduce the computational effort, the second improved scheme is further presented. In this method, the conservative variables and heat flux at the cell interface are approximated by a simple average of those at the left and right cells of cell interface. As compared with the conventional DVM, the improved methods only use different ways to reconstruct distribution function at the cell interface, and the basic procedure for updating the distribution function at cell center is still retained.

Accordingly, the inherent simplicity of the conventional DVM is well kept in the improved schemes. To investigate the performances of different methods in terms of accuracy, efficiency, and stability, a comparative study is then performed in this work by simulating several flow problems varied from low to high speed and from continuum to free molecular flow regime.

2 | DISCRETE VELOCITY METHOD

2.1 | Discrete velocity Boltzmann equation

The DVM is intended to solve the Boltzmann equation in the discretized particle velocity space, which is generally called the DVBE. In order to simulate flows with different Prandtl number, the DVBE with Shakhov model³⁸ is considered

$$\frac{\partial f_\alpha}{\partial t} + \xi_\alpha \cdot \nabla f_\alpha = \frac{f_\alpha^S - f_\alpha}{\tau}, \quad (1)$$

where f_α and f_α^S are the discrete distribution function and its equilibrium state along the direction of discrete velocity ξ_α , ($\alpha = 1, \dots, N_V$, where N_V is the number of discrete particle velocity). τ is the collision time scale. For the Shakhov model, the equilibrium state has a form of

$$f^S = f^{eq} \left[1 + (1 - Pr) \frac{\mathbf{c} \cdot \mathbf{q}}{5pRT} \left(\frac{c^2}{RT} - 5 \right) \right]. \quad (2)$$

Here, f^{eq} is the Maxwellian distribution function given by

$$f^{eq} = \frac{\rho}{(2\pi RT)^{3/2}} \exp \left[-\frac{c^2}{2RT} \right]. \quad (3)$$

Pr is the Prandtl number, $\mathbf{c} = \xi - \mathbf{u}$ is the peculiar velocity of particle, \mathbf{u} is the velocity of mean flow, \mathbf{q} is the heat flux, ρ is the density, p is the pressure, T is the temperature, and R is the gas constant. Note that, in this work, the vector is expressed by the bold style and its magnitude is represented by the italic style (such as $c = |\mathbf{c}|$).

The conservative flow variables \mathbf{W} , heat flux \mathbf{q} , and stress tensor $\bar{\tau}$ can be obtained by taking moments of f_α as follows:

$$\mathbf{W} = (\rho, \rho \mathbf{u}, \rho E)^T = \langle \boldsymbol{\psi} f \rangle_\alpha \quad (4)$$

$$\mathbf{q} = \frac{1}{2} \langle \mathbf{c} c^2 f \rangle_\alpha \quad (5)$$

$$\bar{\tau} = \langle \mathbf{c} \mathbf{c} f \rangle_\alpha - p \bar{\mathbf{I}}, \quad (6)$$

where $\boldsymbol{\psi} = (1, \xi, \xi^2/2)^T$ is the moment, E is the total energy, and $\bar{\mathbf{I}}$ is the unit tensor. The symbol $\langle f \rangle_\alpha$ denotes the quadrature of f in the discrete particle velocity space, ie, the summation, $\langle f \rangle_\alpha = \sum_{\alpha=1}^{N_V} w_\alpha f_\alpha$, where w_α is the associated quadrature weight at the discrete particle velocity point ξ_α . In this work, the Gauss-Hermite quadrature and Newton-Cotes quadrature will be adopted.

2.2 | DVM for solving DVBE

Since the aim of this work is to assess the performance of different solution reconstructions at cell interface in DVM for simulation of flows in all flow regimes, we would like to make a fair comparison between the schemes while keeping the implementation as simple as possible. A natural way to solve DVBE is the standard explicit DVM,^{22,24,39} in which the collision term is discretized explicitly. If the explicit Euler method is used for temporal discretization, Equation (1) can be discretized as

$$\frac{f_\alpha^{n+1} - f_\alpha^n}{\Delta t^n} + \xi_\alpha \cdot \nabla f_\alpha^n = \frac{f_\alpha^{S,n} - f_\alpha^n}{\tau^n}, \quad (7)$$

where the superscript n represents the current time level. Δt is the time interval, which is restrained by the following conditions^{22,39}:

$$\Delta t^n = \min \{ \Delta t_{\text{CFL}}, \tau^n \} \quad (8a)$$

$$\Delta t_{\text{CFL}} = \sigma \frac{\Delta x}{\xi_{\text{max}} + c_s}. \quad (8b)$$

Here, σ is the Courant-Friedrichs-Lewy (CFL) number. ξ_{\max} is the maximum discrete particle velocity, Δx is the grid spacing, and c_s is the sound speed.

To facilitate the simulation of flows with curved boundary, the FVM is utilized to discretize Equation (7) in this work. Integrating Equation (7) over a control volume V yields

$$\frac{V}{\Delta t^n} (f_\alpha^{n+1} - f_\alpha^n) + \int_{\partial V} \mathbf{n} \cdot \xi_\alpha f_{\partial V, \alpha}^n dS = \frac{V}{\tau^n} (f_\alpha^{S, n} - f_\alpha^n), \quad (9)$$

where \mathbf{n} denotes the outward normal vector on the surface of the control volume, and ∂V represents the surface of the control volume. The second term on the left-hand side of Equation (9) is the numerical flux of DVBE at the cell interface. For simplicity, this flux is denoted as

$$\mathbf{F}_{ij, \alpha}^s = \xi_\alpha f_{ij, \alpha}^n. \quad (10)$$

Here, $\mathbf{F}_{ij, \alpha}^s$ is the numerical flux at the cell interface shared by cell i and cell j . $f_{ij, \alpha}^n$ is the distribution function at the cell interface, which should be reconstructed from known values at neighboring cell centers i and j .

By using Equation (9), for grid cell i , the distribution function at cell center can be marched to a new time level $n + 1$ via

$$f_{i, \alpha}^{n+1} = \frac{\tau_i^n - \Delta t_i^n}{\tau_i^n} f_{i, \alpha}^n + \frac{\Delta t_i^n}{\tau_i^n} f_{i, \alpha}^{S, n} - \frac{\Delta t_i^n}{V_i} \sum_{j \in N(i)} \mathbf{n}_{ij} \cdot \mathbf{F}_{ij, \alpha}^s S_{ij}, \quad (11)$$

where $N(i)$ denotes the set of neighboring cells of cell i , S_{ij} is the area of the interface shared by cell i and cell j , and \mathbf{n}_{ij} is the normal vector of the cell interface directing from cell i to cell j . After that, the conservative flow variables, heat flux, and stress tensor can be updated by Equations (4)-(6). It can be seen from Equation (11) that the key to evolve the distribution function at cell center is the calculation of numerical flux at the cell interface, $\mathbf{F}_{ij, \alpha}^s$. Furthermore, as shown in Equation (10), the key to calculate $\mathbf{F}_{ij, \alpha}^s$ is to reconstruct the distribution function at the cell interface, $f_{ij, \alpha}^n$. This issue will be discussed in the following text.

2.3 | Conventional method for calculation of $f_{ij, \alpha}^n$

In the conventional DVM, the distribution function at the cell interface is actually calculated by the local solution of the following collisionless Boltzmann equation with a piecewise constant distribution for the distribution function:

$$\frac{\partial f_\alpha}{\partial t} + \xi_\alpha \cdot \nabla f_\alpha = 0 \quad (12a)$$

$$f(\mathbf{x}, \xi_\alpha, 0) = \begin{cases} f_{ij, \alpha}^{L, n} & \mathbf{n}_{ij} \cdot (\mathbf{x}_{ij} - \mathbf{x}) \geq 0 \\ f_{ij, \alpha}^{R, n} & \mathbf{n}_{ij} \cdot (\mathbf{x}_{ij} - \mathbf{x}) < 0, \end{cases} \quad (12b)$$

where $\mathbf{x}_{ij} \in \partial V$ is the location of the midpoint on cell interface shared by cell i and cell j . $f_{ij, \alpha}^{L, n}$ and $f_{ij, \alpha}^{R, n}$ are the piecewise constant distributions at the left and right sides of cell interface, which can be obtained by interpolation scheme. In this work, the second-order interpolation scheme with van Leer slope limiter function is adopted⁴⁰

$$\begin{aligned} f_{ij, \alpha}^{L, n} &= f_{i, \alpha}^n + (\mathbf{x}_{ij} - \mathbf{x}_i) \cdot \boldsymbol{\sigma}_{i, \alpha}^n \\ f_{ij, \alpha}^{R, n} &= f_{j, \alpha}^n + (\mathbf{x}_{ij} - \mathbf{x}_j) \cdot \boldsymbol{\sigma}_{j, \alpha}^n. \end{aligned} \quad (13)$$

Here, \mathbf{x}_i and \mathbf{x}_j are the coordinates of cell centers of cell i and cell j , respectively. $\boldsymbol{\sigma}_{i, \alpha}^n$ and $\boldsymbol{\sigma}_{j, \alpha}^n$ are the slopes with the slope limiter of $f_{i, \alpha}^n$ and $f_{j, \alpha}^n$.

The local solution of Equation (12a) at the cell interface \mathbf{x}_{ij} yields

$$f_{ij, \alpha}^n = f(\mathbf{x}_{ij}, \xi_\alpha, \Delta t_p) = f(\mathbf{x}_{ij} - \xi_\alpha \Delta t_p, \xi_\alpha, 0). \quad (14)$$

Here, Δt_p is a virtual time step size used in the solution reconstruction. In the conventional DVM, Δt_p has nothing to do with the local solution since a piecewise constant distribution for the distribution function at the cell interface is utilized. By substituting Equation (12b) into Equation (14), we have

$$f_{ij, \alpha}^n = H(\mathbf{n}_{ij} \cdot \xi_\alpha) f_{ij, \alpha}^{L, n} + [1 - H(\mathbf{n}_{ij} \cdot \xi_\alpha)] f_{ij, \alpha}^{R, n}, \quad (15)$$

where $H(\mathbf{n}_{ij} \cdot \xi_\alpha)$ is the Heaviside function, $H(\mathbf{n}_{ij} \cdot \xi_\alpha) = 1$ for $\mathbf{n}_{ij} \cdot \xi_\alpha \geq 0$ and $H(\mathbf{n}_{ij} \cdot \xi_\alpha) = 0$ for $\mathbf{n}_{ij} \cdot \xi_\alpha < 0$. The illustration of the local solution of collisionless Boltzmann equation is depicted in Figure 1. Once $f_{ij, \alpha}^n$ is obtained, the numerical

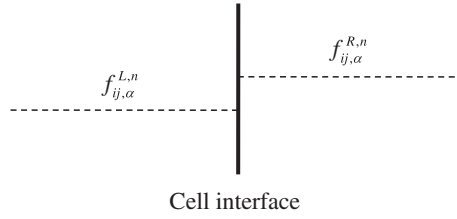


FIGURE 1 Distribution function at the cell interface determined by the local solution of collisionless Boltzmann equation

flux at the cell interface can be calculated straightforwardly by substituting Equation (15) into Equation (10), and the distribution function at cell center can be marched to a new time level $n + 1$ via Equation (11).

2.4 | Improved Scheme I for calculation of $f_{ij,a}^n$

As shown in Section 2.3, the collision effect on the calculation of distribution function at the cell interface $f_{ij,a}^n$ is ignored in the conventional DVM. In high Knudsen number flows, the particle collision effect is not significant. As a result, the conventional method for calculation of $f_{ij,a}^n$ is a good approximation. However, in the continuum flow regime, the conventional model would produce a large numerical dissipation because the particle collision happens frequently.

To overcome the above defect, an improved method is presented in this section. In the method, the distribution function at the cell interface is reconstructed physically by the local solution of Boltzmann equation with Shakhov model (Equation (1)) and the following initial distribution:

$$f(\mathbf{x}, \xi_\alpha, 0) = \begin{cases} f_{i,\alpha}^n + (\mathbf{x} - \mathbf{x}_i) \cdot \boldsymbol{\sigma}_{i,\alpha}^n, & \mathbf{n}_{ij} \cdot (\mathbf{x}_{ij} - \mathbf{x}) \geq 0 \\ f_{j,\alpha}^n + (\mathbf{x} - \mathbf{x}_j) \cdot \boldsymbol{\sigma}_{j,\alpha}^n, & \mathbf{n}_{ij} \cdot (\mathbf{x}_{ij} - \mathbf{x}) < 0. \end{cases} \quad (16)$$

The initial distribution of Equation (16) is depicted in Figure 2. Note that the piecewise linear distribution is assumed in the improved scheme, which is different from the piecewise constant distribution shown in Equation (12b) and Figure 1.

For ease of implementation, the first-order implicit scheme is utilized to discretize the collision term in reconstructing the local solution of DVBE with Shakhov model at the cell interface \mathbf{x}_{ij} . As a result, we have

$$\begin{aligned} f_{ij,a}^n &= f(\mathbf{x}_{ij}, \xi_\alpha, \Delta t_p) \\ &= f(\mathbf{x}_{ij} - \xi_\alpha \Delta t_p, \xi_\alpha, 0) + \frac{\Delta t_p}{\tau_{ij}} [f^S(\mathbf{x}_{ij}, \xi_\alpha, \Delta t_p) - f(\mathbf{x}_{ij}, \xi_\alpha, \Delta t_p)], \end{aligned} \quad (17)$$

where $\tau_{ij} = \tau(\mathbf{x}_{ij}, \Delta t_p)$ is the collision time scale at the cell interface. In Equation (17), the principle for the choice of Δt_p is that the location of $f(\mathbf{x}_{ij} - \xi_\alpha \Delta t_p, \xi_\alpha, 0)$ must be within the cell of the interface in order to avoid extrapolation. The effect of Δt_p on the numerical solution has been investigated comprehensively by Shu et al.⁴¹ It was found that the value of Δt_p has almost no effect on the solution accuracy, as long as it satisfies the above constraint. For simplicity, $\Delta t_p = (\Delta t_i + \Delta t_j)/4$ is used in this work. Here, Δt_i and Δt_j are the time step sizes determined by Equation (8) for cell i and cell j , respectively. Since Δt_i and Δt_j are restrained by CFL condition, the selected Δt_p can avoid extrapolation automatically. The second term on the right-hand side of Equation (17) is the collision term, which represents the collision effect at the cell interface. Equation (17) can be rearranged as

$$f_{ij,a}^n = \frac{\tau_{ij}}{\tau_{ij} + \Delta t_p} f(\mathbf{x}_{ij} - \xi_\alpha \Delta t_p, \xi_\alpha, 0) + \frac{\Delta t_p}{\tau_{ij} + \Delta t_p} f^S(\mathbf{x}_{ij}, \xi_\alpha, \Delta t_p). \quad (18)$$

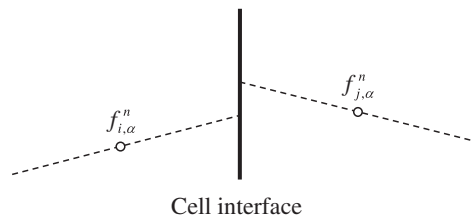


FIGURE 2 Distribution function at the cell interface determined by the local solution of Boltzmann equation with Shakhov model. The symbol “o” denotes the location of cell center

It can be seen from Equation (18) that the distribution function at the cell interface is a linear combination of the distribution function at the surrounding points of cell interface $f(\mathbf{x}_{ij} - \xi_\alpha \Delta t_p, \xi_\alpha, 0)$ and the equilibrium state on the cell interface $f^S(\mathbf{x}_{ij}, \xi_\alpha, \Delta t_p)$. By using the initial distribution of Equation (16), the distribution function at the surrounding points of cell interface can be computed by

$$f(\mathbf{x}_{ij} - \xi_\alpha \Delta t_p, \xi_\alpha, 0) = H(\mathbf{n}_{ij} \cdot \xi_\alpha) \left(f_{i,\alpha}^n + (\mathbf{x}_{ij} - \xi_\alpha \Delta t_p - \mathbf{x}_i) \cdot \boldsymbol{\sigma}_{i,\alpha}^n \right) + [1 - H(\mathbf{n}_{ij} \cdot \xi_\alpha)] \left(f_{j,\alpha}^n + (\mathbf{x}_{ij} - \xi_\alpha \Delta t_p - \mathbf{x}_j) \cdot \boldsymbol{\sigma}_{j,\alpha}^n \right). \quad (19)$$

In order to calculate the equilibrium distribution function on the cell interface, the conservative flow variables $\mathbf{W}(\mathbf{x}_{ij}, \Delta t_p)$ and heat flux $\mathbf{q}(\mathbf{x}_{ij}, \Delta t_p)$ at the same physical location have to be determined in advance. Taking conservative moments of Equation (17) and according to the compatibility condition, we have

$$\mathbf{W}(\mathbf{x}_{ij}, \Delta t_p) = \langle \boldsymbol{\psi} f(\mathbf{x}_{ij} - \xi \Delta t_p, \xi, 0) \rangle_\alpha. \quad (20)$$

It can be seen from Equation (20) that the conservative flow variables at the cell interface are determined by the distribution function at the surrounding points of cell interface. Once $\mathbf{W}(\mathbf{x}_{ij}, \Delta t_p)$ is obtained, the primitive flow variables and collision time scale τ_{ij} at the cell interface can then be calculated straightforwardly. Furthermore, by substituting Equation (18) into Equation (5), we have

$$\mathbf{q}(\mathbf{x}_{ij}, \Delta t_p) = \frac{\tau_{ij}}{\tau_{ij} + Pr \Delta t_p} \left\langle \frac{1}{2} \mathbf{c} c^2 f(\mathbf{x}_{ij} - \xi \Delta t_p, \xi, 0) \right\rangle_\alpha. \quad (21)$$

Finally, the equilibrium distribution function at the cell interface $f^S(\mathbf{x}_{ij}, \xi_\alpha, \Delta t_p)$ can be computed by substituting $\mathbf{W}(\mathbf{x}_{ij}, \Delta t_p)$ and $\mathbf{q}(\mathbf{x}_{ij}, \Delta t_p)$ into Equation (2).

As compared with the conventional method, the collision effect is incorporated into the evaluation of distribution function at the cell interface in the improved scheme. This improvement makes the present scheme be more accurate than the conventional DVM in the continuum flow regime, which will be demonstrated in the numerical examples presented in Section 3. However, some extra computational efforts for determining the conservative flow variables, heat flux, and equilibrium distribution function at the cell interface, which relate to the moments of distribution functions in the whole particle velocity space, are required by the improved method. These manipulations trade-off its computational efficiency in simulation. For the convenience of elaboration, we denote this improved method as “Scheme I” in the following text.

2.5 | Improved Scheme II for calculation of $f_{ij,a}^n$

In Scheme I, to incorporate the collision effect into the solution reconstruction at cell interface, the moments of distribution functions in the whole particle velocity space need to be computed. The computational cost of this manipulation is related to the scale of discrete velocity point. To reduce the computational effort, and at the same time retain the collision effect in evaluating of distribution function at the cell interface, the second improved scheme is developed in this section. In the method, the conservative flow variables and heat flux at the cell interface are approximated by

$$\mathbf{W}(\mathbf{x}_{ij}, \Delta t_p) = \frac{1}{2} (\mathbf{W}_i + \mathbf{W}_j) \quad (22)$$

$$\mathbf{q}(\mathbf{x}_{ij}, \Delta t_p) = \frac{1}{2} (\mathbf{q}_i + \mathbf{q}_j), \quad (23)$$

where \mathbf{W}_i and \mathbf{W}_j are the conservative variables at cell centers of cell i and cell j , respectively. \mathbf{q}_i and \mathbf{q}_j are the heat flux at cell centers of cell i and cell j . Once $\mathbf{W}(\mathbf{x}_{ij}, \Delta t_p)$ and $\mathbf{q}(\mathbf{x}_{ij}, \Delta t_p)$ are determined, the rest of implementation is the same as Scheme I. To differ it from Scheme I, the current scheme is denoted as “Scheme II” in this work.

3 | NUMERICAL EXAMPLES

Since the numerical quadrature is utilized to fulfill the calculation of conservative variables in DVM, the fundamental property of mass, momentum, and energy conservation may not be satisfied accurately. Hence, the numerical error will accumulate and prevent the system from converging to its physical solution. To overcome this drawback, a large number

of studies have been carried out for both Bhatnagar-Gross-Krook (BGK) model^{21,26} and Shakhov model.^{12,42-44} For Shakhov model, the conservation condition can be written as¹²

$$\langle \Psi_1(f^S - f) \rangle_\alpha = (0, \mathbf{0}, 0, -Pr\mathbf{q})^T, \quad (24)$$

where $\Psi_1 = (1, \xi, \xi^2/2, \mathbf{c}c^2/2)^T$. Equation (24) is actually a nonlinear system for $\mathbf{h} = (\rho, \mathbf{u}, T, \mathbf{q})^T$ because f_α^S is the function of \mathbf{h} as shown in Equation (2). To resolve this nonlinear system, we introduce a function $\Phi(\mathbf{h})$ as follows:

$$\Phi(\mathbf{h}) = \langle \Psi_1(f^S - f) \rangle_\alpha - (0, \mathbf{0}, 0, -Pr\mathbf{q})^T = 0. \quad (25)$$

Equation (25) can then be solved by Newton iterations as²⁶

$$\mathbf{h}^{l+1} = \mathbf{h}^l - \left[\frac{\partial \Phi(\mathbf{h}^l)}{\partial \mathbf{h}^l} \right]^{-1} \Phi(\mathbf{h}^l), \quad l = 1, 2, \dots \quad (26)$$

In this work, to start the iterative process, we set the initial guess \mathbf{h}^1 as the quadrature of f_α given by Equations (4)-(5). As pointed out by Titarev,⁴² one or two iterations are enough since Newton algorithm converges rapidly. In our calculation, the above method is utilized to enforce the conservative property of Shakhov model at each cell and the convergence criterion of Newton iterations is set by the condition that the error of \mathbf{h} at two adjacent iteration steps does not exceed 10^{-10} .

To investigate the accuracy, efficiency, and stability of different solution reconstructions at cell interface in DVM for simulation of flows in all flow regimes, the force-driven Poiseuille flow, lid-driven cavity flow, and hypersonic flow around a cylinder are simulated in this section. Unless otherwise stated, the Prandtl number is taken as $Pr = 2/3$, the specific heat ratio is chosen as $\gamma = 5/3$, and the CFL number is set as $\sigma = 0.9$. In the simulations, the dynamic viscosity μ and collision time scale τ are determined by

$$\mu = \mu_0 \left(\frac{T}{T_0} \right)^w \quad (27)$$

$$\tau = \frac{\mu}{p}, \quad (28)$$

where T_0 and μ_0 are the temperature and dynamic viscosity at the reference state. w is the coefficient related to the intermolecular interaction model. In addition, all the computations were done on a personal computer with a processor of Intel(R) Xeon(R) E5-2687 CPU@3.0 GHz, and no parallel computation is adopted here.

Case 1: Force-driven Poiseuille flow

The first test case is the force-driven Poiseuille flow with different Knudsen numbers.^{23,45,46} This problem can be considered as a viscous fluid flow between two infinite parallel plates with temperature of $T_0 = 273$ K separated by a distance of L in the y -direction. An external force is exerted in the x -direction, so that Equation (1) can be rewritten as

$$\frac{\partial f_\alpha}{\partial t} + \xi_\alpha \cdot \nabla f_\alpha = \frac{f_\alpha^S - f_\alpha}{\tau} + F_{\alpha,x}, \quad (29)$$

where $F_{\alpha,x}$ is the force term given by

$$F_{\alpha,x} = -G \frac{\partial f_\alpha^S}{\partial \xi_{\alpha,x}}. \quad (30)$$

Here, $\xi_{\alpha,x}$ is the x -component of the discrete particle velocity ξ_α , and G is the magnitude of the external acceleration. For simplicity, the Prandtl number is set as $Pr = 1$ in current simulation. As a result, we have

$$\frac{\partial f_\alpha^S}{\partial \xi_{\alpha,x}} = -\frac{\xi_{\alpha,x} - u_x}{RT} f_\alpha^{eq}, \quad (31)$$

where u_x is the x -component of the velocity of mean flow \mathbf{u} .

The Knudsen number of this test case is defined as

$$Kn = \lambda_0/L. \quad (32)$$

Here, λ_0 is the particle mean free path at the reference state given by

$$\lambda_0 = \frac{\mu_0}{\rho_0} \sqrt{\frac{\pi}{2RT_0}}, \quad (33)$$

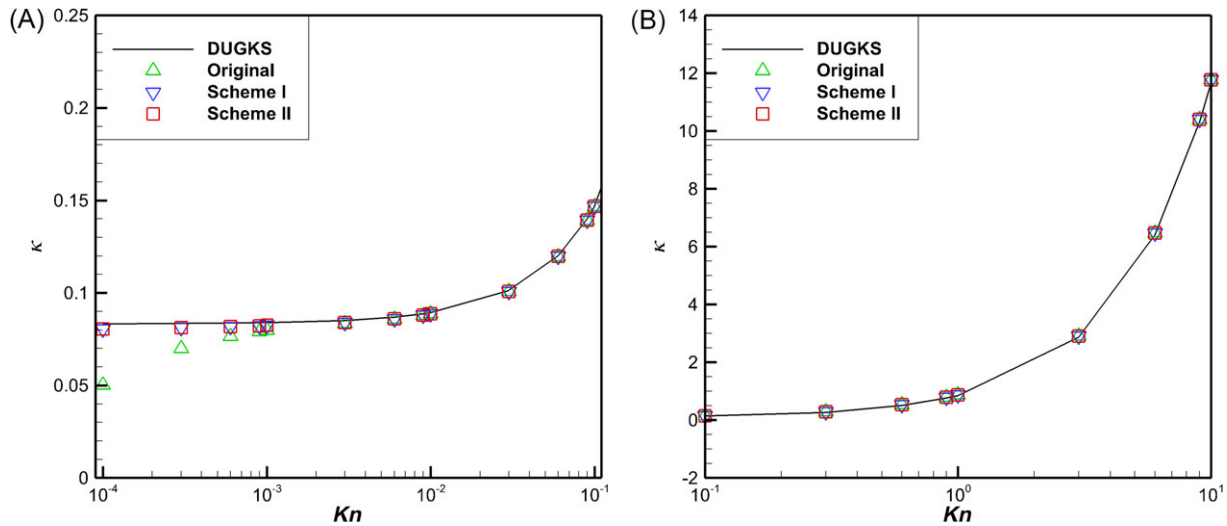


FIGURE 3 Apparent gas permeability for Poiseuille flow at different Kn . (A) $10^{-4} \leq Kn \leq 0.1$. (B) $0.1 \leq Kn \leq 10$. DUGKS, discrete unified gas kinetic scheme [Colour figure can be viewed at wileyonlinelibrary.com]

where ρ_0 is the density at the reference state. For this test example, the apparent gas permeability κ is often used to quantify the simulation results, which is defined as

$$\kappa = \frac{Kn}{\sqrt{\pi}GL^2} \int_0^L u dy. \quad (34)$$

In the present simulation, the computational domain in y -direction is discretized uniformly by 40 cells; the isothermal boundary condition is implemented on the bottom and upper walls; and the periodic boundary condition is adopted on the left and right boundaries. The convergence criterion is set by the condition that the error of κ at two adjacent iteration steps does not exceed 10^{-10} .

Consistent with previous study,²³ in our simulation, the hard-sphere (HS) model is utilized to calculate the dynamic viscosity, where the exponent w in Equation (27) is 0.5. The Knudsen number is varied from $Kn = 10^{-4}$ to 10, which covers the free molecular flow regime ($Kn \geq 10$), transition flow regime ($10^{-1} \leq Kn < 10$), slip flow regime ($10^{-2} \leq Kn < 10^{-1}$), and continuum flow regime ($Kn < 10^{-2}$). The magnitude of the external acceleration is taken as $G = 10^{-5}$ for the case of $10^{-4} \leq Kn < 10^{-3}$, $G = 10^{-4}$ for $10^{-3} \leq Kn < 10^{-2}$, $G = 10^{-3}$ for $10^{-2} \leq Kn < 10^{-1}$, and $G = 10^{-2}$ for $10^{-1} \leq Kn$. For discretization of the particle velocity space, the Gauss-Hermite quadrature with 8×8 mesh points and 28×28 mesh points are respectively used in the cases of $Kn < 10^{-2}$ and $10^{-2} \leq Kn < 1$, and the Newton-Cotes quadrature with 201×201 mesh points and 301×301 mesh points uniformly distributed in $[-4\sqrt{2RT_0}, 4\sqrt{2RT_0}] \times [-4\sqrt{2RT_0}, 4\sqrt{2RT_0}]$ are adopted in the cases of $1 \leq Kn < 10$ and $Kn = 10$.

Figure 3 shows the apparent gas permeability for Poiseuille flow in different flow regimes. Also displayed in this figure is the result obtained by DUGKS.²³ It can be seen from Figure 3B that the simulation results of three different methods for solution reconstructions at the cell interface are basically the same and they compare well with that of DUGKS in the free molecular flow regime, transition flow regime and slip flow regime. However, in the continuum flow regime, the results of improved methods (Scheme I and Scheme II) are better than that of the original model as shown in Figure 3A, and the improvement becomes more evident as the Knudsen number is decreased. This observation can also be validated via Figure 4, which depicts the comparison of velocity profiles along the channel cross-section calculated by different schemes. Note that, in this Figure, the velocity is normalized by $\sqrt{2RT_0}$. For the test cases of $Kn = 0.1$, 1, and 10, the results of three schemes and DUGKS compare well with each other, while for the test case of $Kn = 10^{-3}$, the simulation results of two improved schemes are closer to that of DUGKS than the original one. This test example well demonstrates that the developed methods for solution reconstruction with particle collision effect can effectively improve the solution accuracy of conventional DVM in the continuum flow regime.

Case 2: Lid-driven cavity flow

To compare the solution accuracy and computational efficiency of different methods in the two-dimensional case, the lid-driven cavity flow with various Knudsen and Reynolds numbers is simulated. This problem has been widely studied both in the rarefied flow regime^{13,27,33,34,47-49} and in the continuum flow regime.⁵⁰⁻⁵⁴ The computational domain of this test

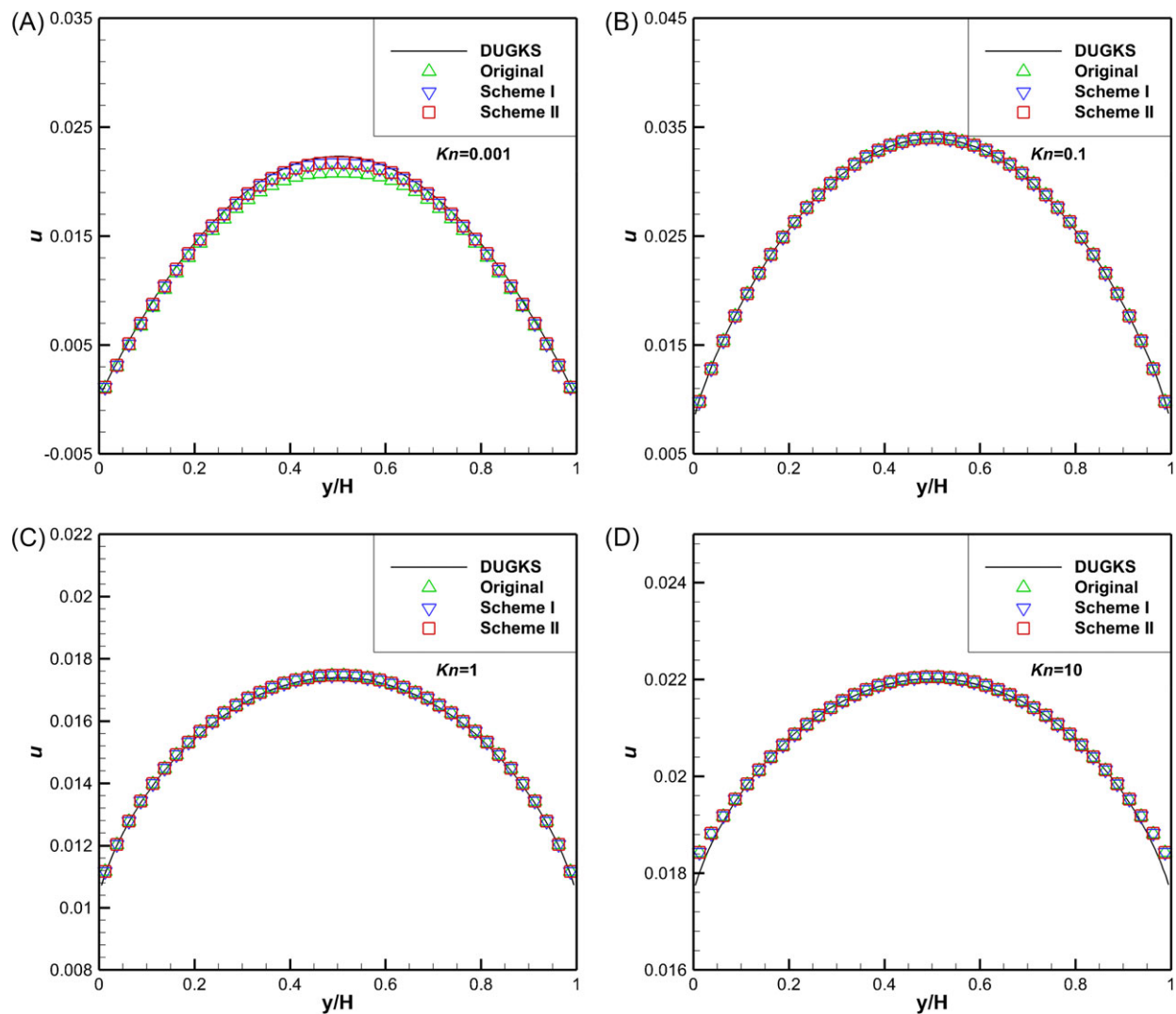


FIGURE 4 Velocity profiles along the channel cross-section at (A) $Kn = 10^{-3}$, (B) $Kn = 0.1$, (C) $Kn = 1$, and (D) $Kn = 10$. DUGKS, discrete unified gas kinetic scheme [Colour figure can be viewed at [wileyonlinelibrary.com](#)]

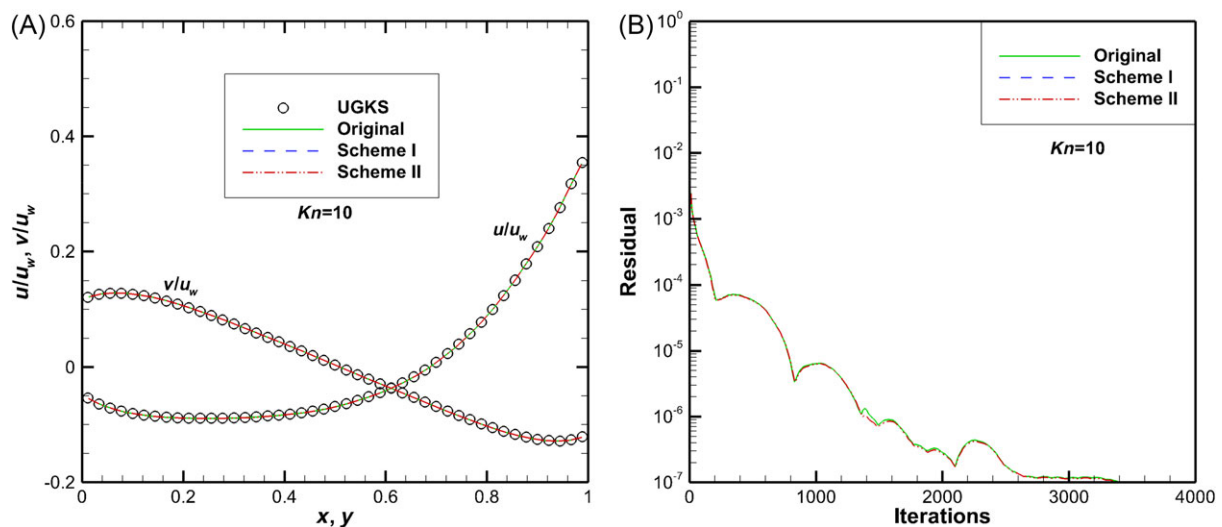


FIGURE 5 Lid-driven cavity flow at $Kn = 10$. (A) Velocity profiles along the central lines. (B) Convergence history. UGKS, unified gas kinetic scheme [Colour figure can be viewed at [wileyonlinelibrary.com](#)]

example is a square cavity with the edge length of L . At the top wall, the temperature and velocity are fixed at $T_0 = 273$ K and $u_0 = 0.15\sqrt{2RT_0}$, respectively. Remaining three walls are stationary and in constant temperature of T_0 . For the rarefied case, the reference viscosity is calculated by

$$\frac{\mu_0}{L} = \frac{5\rho_0(2\pi RT_0)^{1/2}}{16} Kn, \quad (35)$$

and for the continuous case, the reference viscosity is determined by

$$\mu_0 = \frac{\rho_0 u_0 L}{Re}, \quad (36)$$

where Re is the Reynolds number. In the simulation, the variable HS model is utilized, which gives $w = 0.81$ in Equation (27). For discretization of the physical space, the uniform mesh with 40×40 cells is used for the rarefied case, and the uniform mesh with 100×100 cells is utilized for the continuous case. The convergence criteria for the rarefied and continuous cases are set by the condition that the maximum errors of all primitive variables at two adjacent iteration steps do not exceed 10^{-7} and 10^{-8} , respectively.

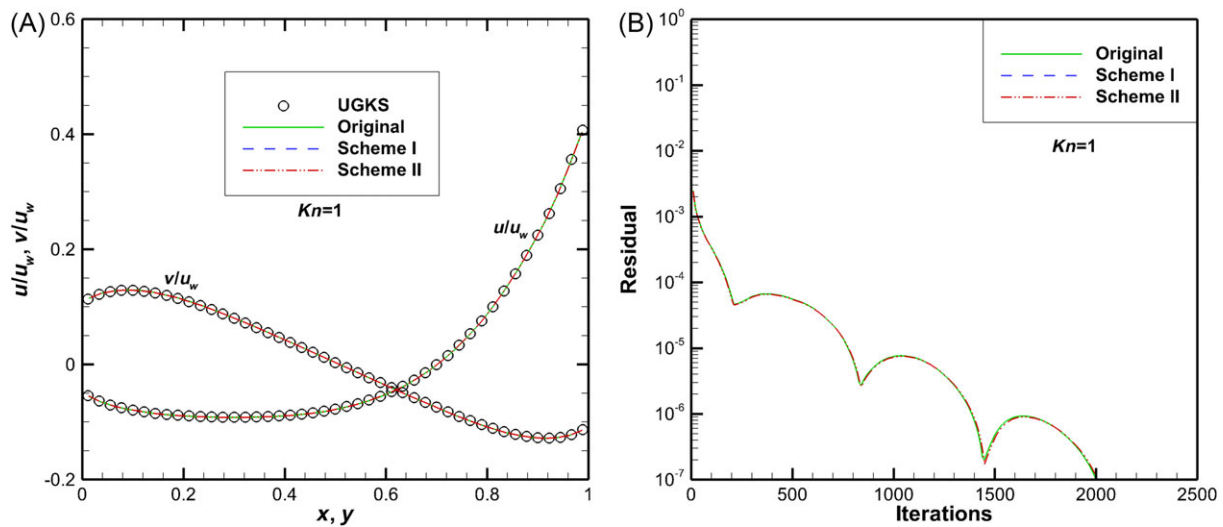


FIGURE 6 Lid-driven cavity flow at $Kn = 1$. (A) Velocity profiles along the central lines. (B) Convergence history. UGKS, unified gas kinetic scheme [Colour figure can be viewed at [wileyonlinelibrary.com](#)]

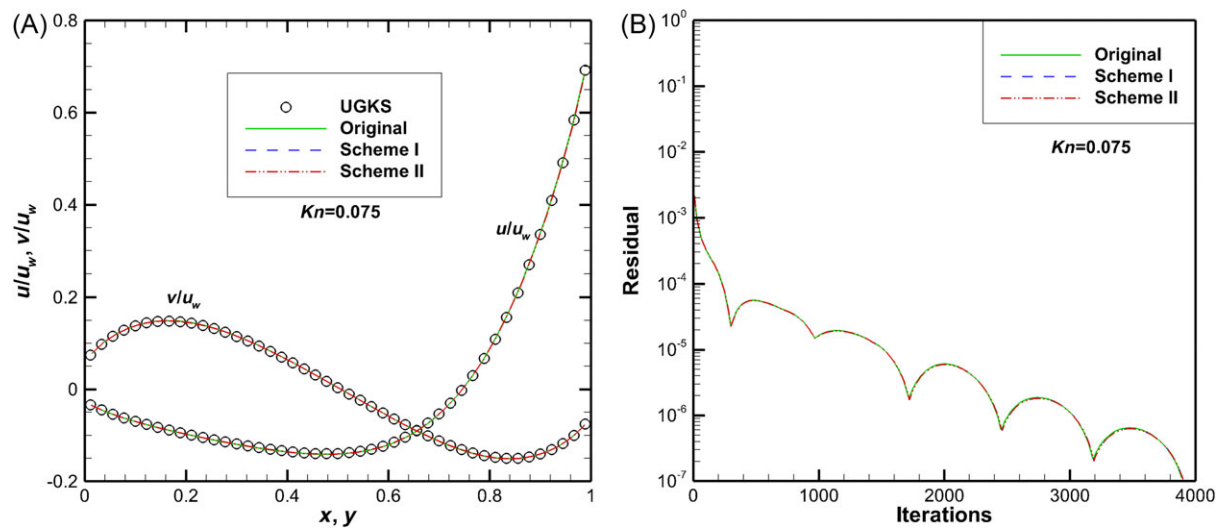


FIGURE 7 Lid-driven cavity flow at $Kn = 0.075$. (A) Velocity profiles along the central lines. (B) Convergence history. UGKS, unified gas kinetic scheme [Colour figure can be viewed at [wileyonlinelibrary.com](#)]

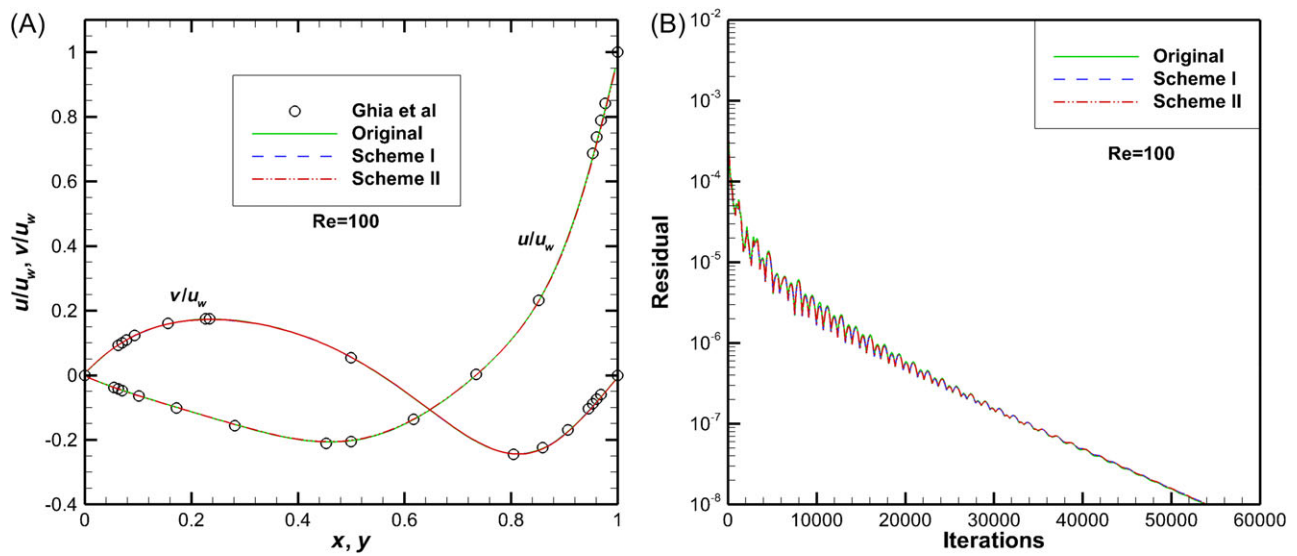


FIGURE 8 Lid-driven cavity flow at $Re = 100$. (A) Velocity profiles along the central lines. (B) Convergence history [Colour figure can be viewed at wileyonlinelibrary.com]

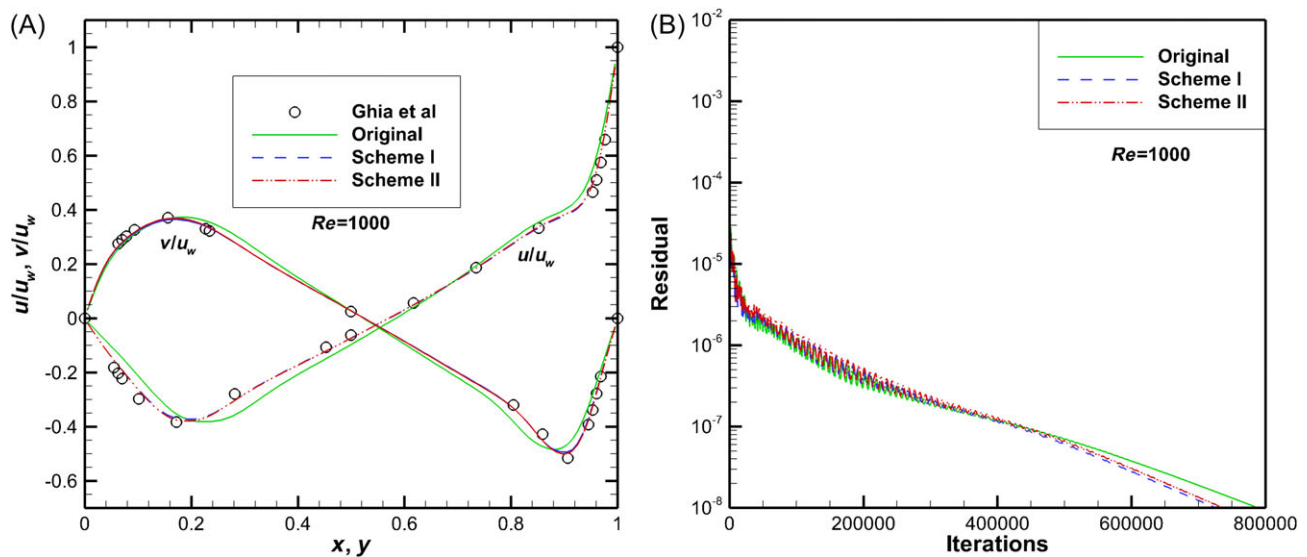


FIGURE 9 Lid-driven cavity flow at $Re = 1000$. (A) Velocity profiles along the central lines. (B) Convergence history [Colour figure can be viewed at wileyonlinelibrary.com]

TABLE 1 Computational time (hours) of different methods for lid-driven cavity flow at different Knudsen and Reynolds numbers

Kn or Re	Original	Scheme I	Scheme II
$Kn = 10$	0.730	1.102	1.051
$Kn = 1$	0.426	0.652	0.618
$Kn = 0.075$	0.092	0.146	0.138
$Re = 100$	1.084	1.628	1.535
$Re = 1000$	15.616	22.123	20.857

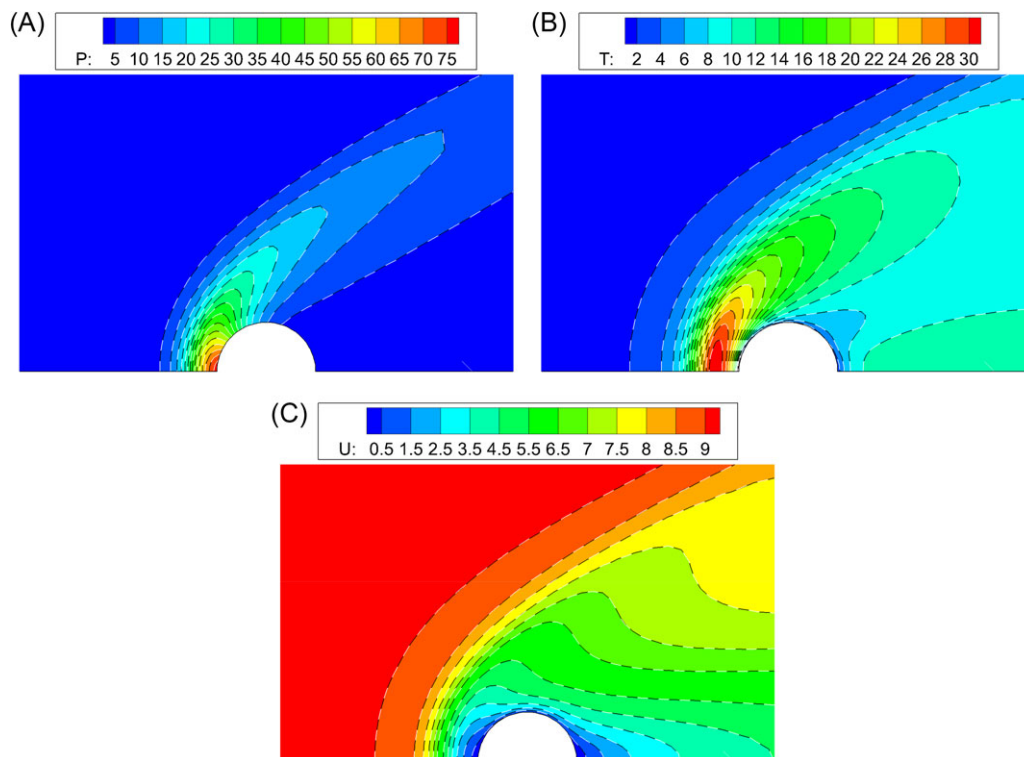


FIGURE 10 Simulation results for hypersonic flow around a cylinder at $Ma = 10$ and $Kn = 0.1$ (Original: colored background with black solid line; Scheme II: white dash line). (A) Pressure contours. (B) Temperature contours. (C) u -velocity contours [Colour figure can be viewed at wileyonlinelibrary.com]

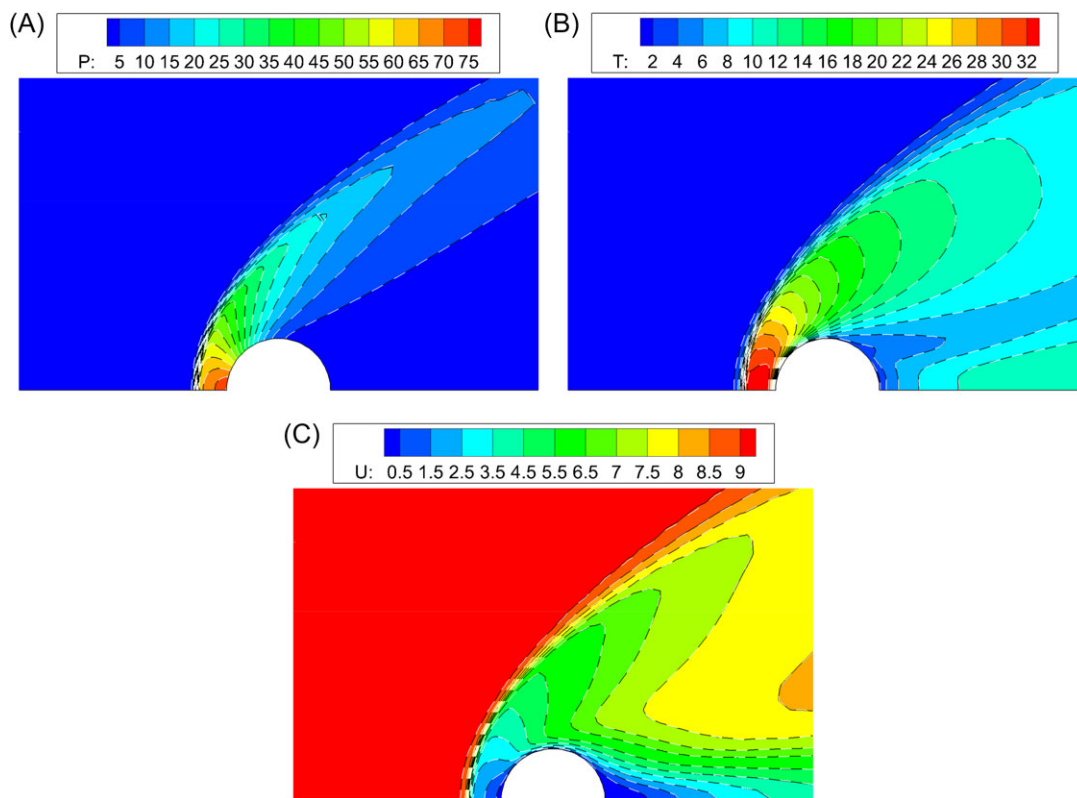


FIGURE 11 Simulation results for hypersonic flow around a cylinder at $Ma = 10$ and $Kn = 0.01$ (Original: colored background with black solid line; Scheme II: white dash line). (A) Pressure contours. (B) Temperature contours. (C) u -velocity contours [Colour figure can be viewed at wileyonlinelibrary.com]

In our simulation, five test cases with three different Knudsen numbers of $Kn = 10$, 1, and 0.075 and two different Reynolds numbers of $Re = 100$ and 1000 are resolved. The test examples of $Kn = 10$, 1, and 0.075 respectively correspond to the free molecular flow regime, transition flow regime, and slip flow regime, and the test cases of $Re = 100$ and 1000 belong to the continuum flow regime. For discretization of the particle velocity space, the Newton-Cotes quadrature with 81×81 mesh points uniformly distributed in $[-4\sqrt{2RT_0}, 4\sqrt{2RT_0}] \times [-4\sqrt{2RT_0}, 4\sqrt{2RT_0}]$ is utilized in the cases of $Kn = 10$ and 1, and the Gauss-Hermite quadrature with 28×28 mesh points and 8×8 mesh points are respectively used in the case of $Kn = 0.075$ and continuum flow. Figures 5 to 9 show the velocity profiles along the central lines and the convergence history for the test cases of $Kn = 10$, 1, and 0.075, and $Re = 100$ and 1000, respectively. It can be observed that both velocity profiles and convergence history for the cases of $Kn = 10$, 1, and 0.075, and $Re = 100$ computed by three different schemes are consistent with each other, and their velocity profiles compare well with those of UGKS⁴⁸ and the benchmark data.⁵⁰ However, for the test case of $Re = 1000$, the velocity profiles obtained by the improved schemes are closer to the benchmark data⁵⁰ than those of the original model. As far as the computational efficiency is concerned, the conventional DVM is more efficient than the improved schemes as reported in Table 1. The reason is that some extra computational efforts regarding to the calculation of conservative variables, heat flux, and equilibrium state at the cell interface are required for the improved schemes. In addition, the computation of Scheme II is relatively efficient as compared with Scheme I since

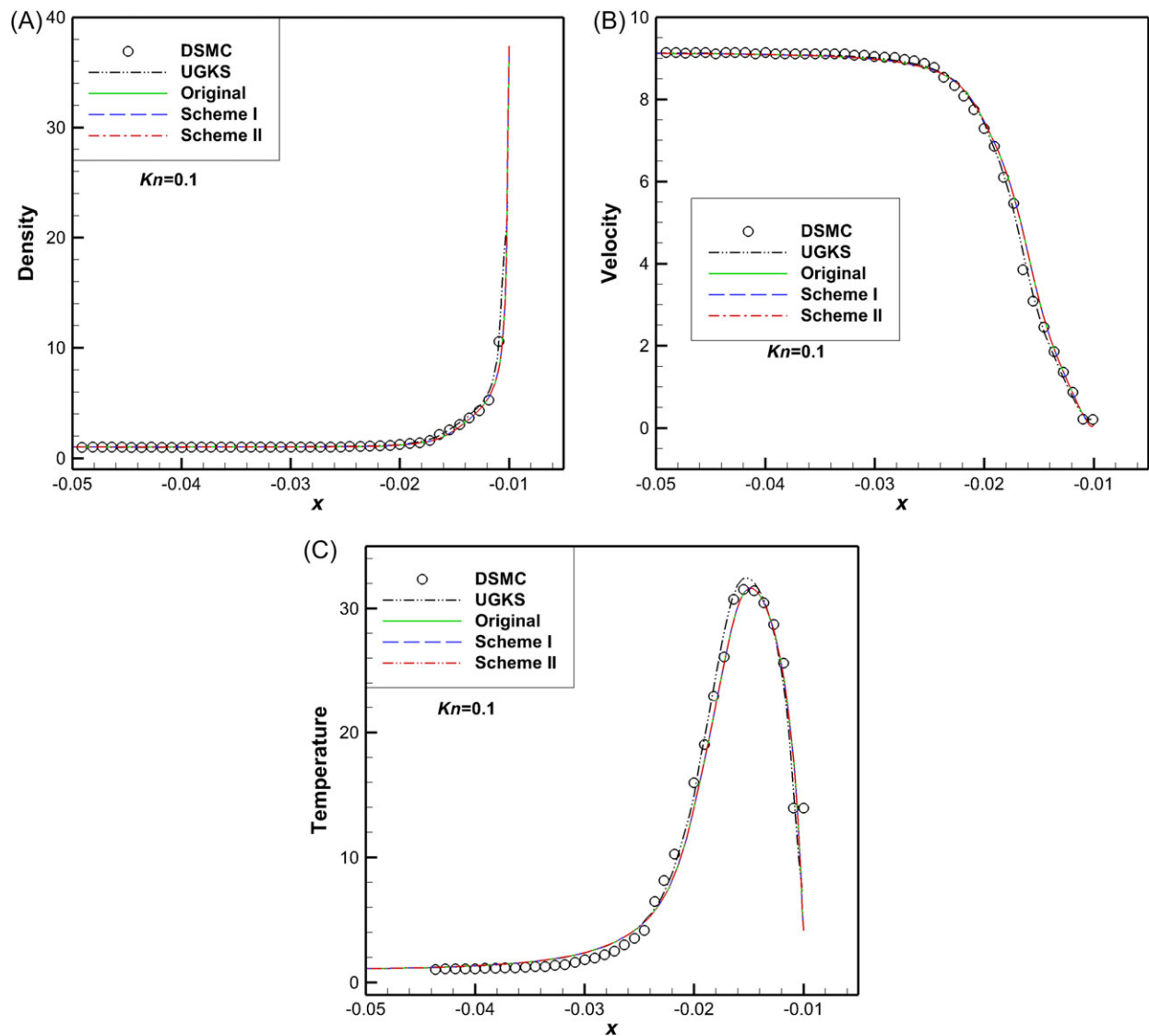


FIGURE 12 Profiles along the stagnation line for hypersonic flow around a cylinder at $Ma = 10$ and $Kn = 0.1$. (A) Density. (B) u -velocity. (C) Temperature. DSMC, direct simulation Monte Carlo; UGKS, unified gas kinetic scheme [Colour figure can be viewed at wileyonlinelibrary.com]

the moments of distribution functions in the whole particle velocity space for computing the conservative variables and heat flux are approximated by a simple average. Overall, the computational time of Scheme II is about 1.3–1.5 times of that of the conventional DVM. This test case further shows that the solution accuracy of the improved schemes is better than that of the conventional DVM in the continuum flow regime, while the latter is more efficient.

Case 3: Hypersonic flow around a cylinder

Hypersonic flows exist widely in aerospace engineering.^{36,55–59} To assess the performance of the improved schemes for high-speed rarefied flows, the hypersonic flow around a cylinder with radius of $R_0 = 0.01$ m at Mach number of $Ma = 10$ and Knudsen numbers of $Kn = 0.1$ and 0.01 is simulated. Consistent with previous study,⁵⁹ in the present work, the reference density for the cases of $Kn = 0.1$ and 0.01 are respectively given as $\rho_0 = 8.585 \times 10^{-5}$ kg/m³ and 8.585×10^{-4} kg/m³. The reference temperature is taken as $T_0 = 273$ K, the temperature of the cylinder is fixed at T_0 , and the reference viscosity is determined by

$$\frac{\mu_0}{R_0} = \frac{15\rho_0(2\pi RT_0)^{1/2}}{2(5-2w)(7-2w)}Kn, \quad (37)$$

where $w = 0.81$ is the coefficient related to the intermolecular interaction model. The CFL number is set as $\sigma = 0.2$ to ensure convergence. Due to symmetry of the flow field, only upper half of the cylinder is considered to reduce the computational

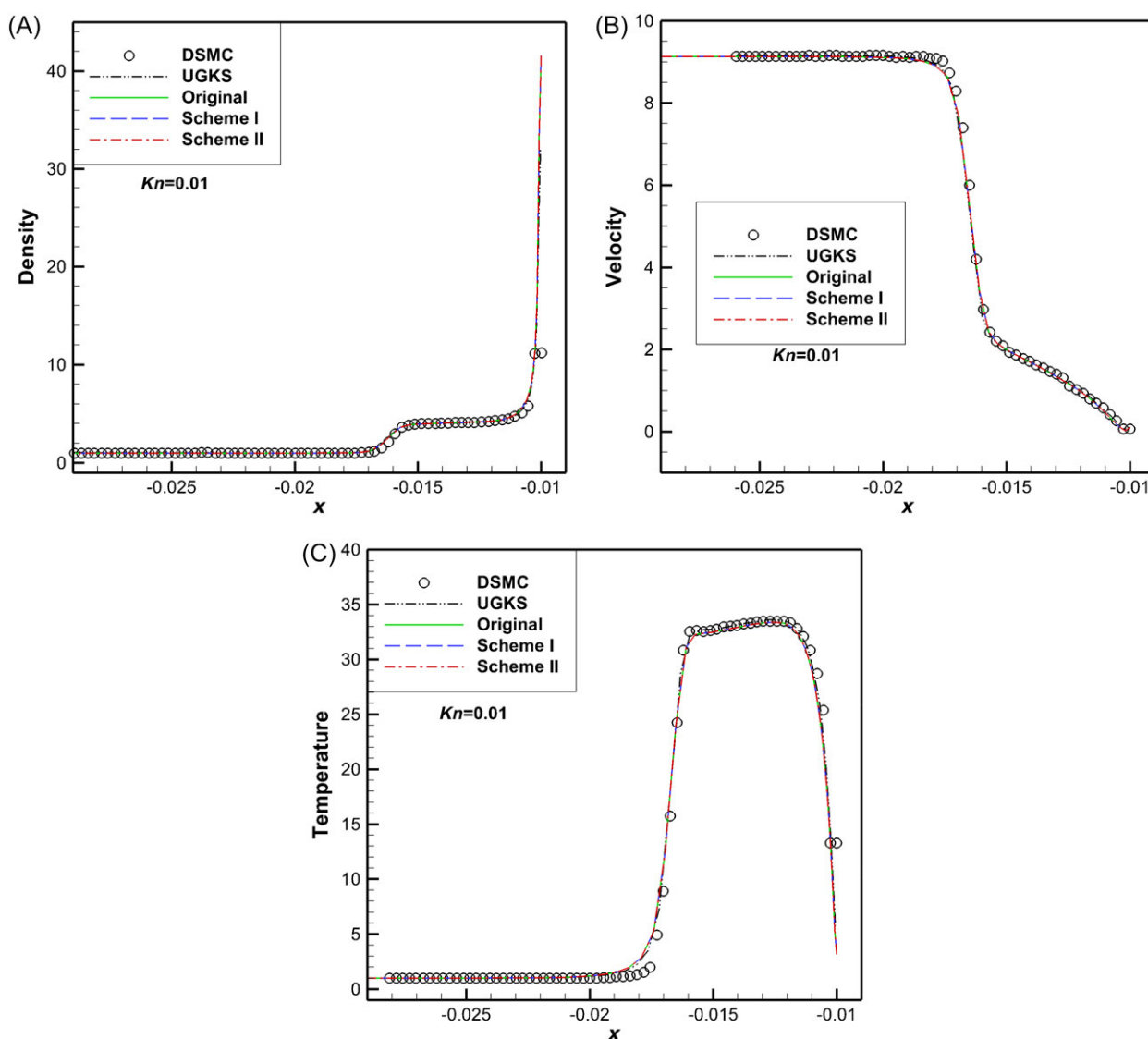


FIGURE 13 Profiles along the stagnation line for hypersonic flow around a cylinder at $Ma = 10$ and $Kn = 0.01$. (A) Density. (B) u -velocity. (C) Temperature. DSMC, direct simulation Monte Carlo; UGKS, unified gas kinetic scheme [Colour figure can be viewed at wileyonlinelibrary.com]

effort. In the calculation, a nonuniform mesh with 60 cells in the circumferential direction and 70 cells in the surface normal direction is used to discretize the physical space. The far-field boundary is put at $11R_0$ away from the center of the cylinder. The distance from the wall to the nearest grid point in the computational domain is taken as $\Delta r = 0.00012$ m and 0.00008 m for the cases of $Kn = 0.1$ and $Kn = 0.01$, respectively. The ratio of mesh spacing along the surface normal direction is controlled by the hyperbolic tangent function. In the particle velocity space, the Newton-Cotes quadrature with 161×161 mesh points uniformly distributed in $[-20\sqrt{2RT_0}, 20\sqrt{2RT_0}] \times [-20\sqrt{2RT_0}, 20\sqrt{2RT_0}]$ is utilized. The convergence criteria are set by the condition that the maximum errors of all primitive variables at two adjacent iteration steps do not exceed 10^{-6} .

The comparison of pressure, temperature, and u -velocity contours computed by the conventional DVM and Scheme II for the cases of $Kn = 0.1$ and 0.01 are shown in Figures 10 and 11, respectively. It can be seen that the results of two schemes are in line with each other. The smaller the Knudsen number, the thinner and steeper the bow shock wave. In Figures 12 and 13, the density, u -velocity, and temperature profiles along the stagnation line in front of the cylinder computed by three different methods for solution reconstruction are compared with those of Yu⁵⁹ obtained by the UGKS with adaptive mesh refinement in the particle velocity space and the direct simulation Monte Carlo (DSMC) method. Further comparisons of the computed surface quantities such as pressure, shear stress, and normal heat flux in our simulation and those obtained by UGKS and DSMC⁵⁹ are carried out in Figures 14 and 15 for the cases of $Kn = 0.1$ and 0.01 , respectively. Overall,

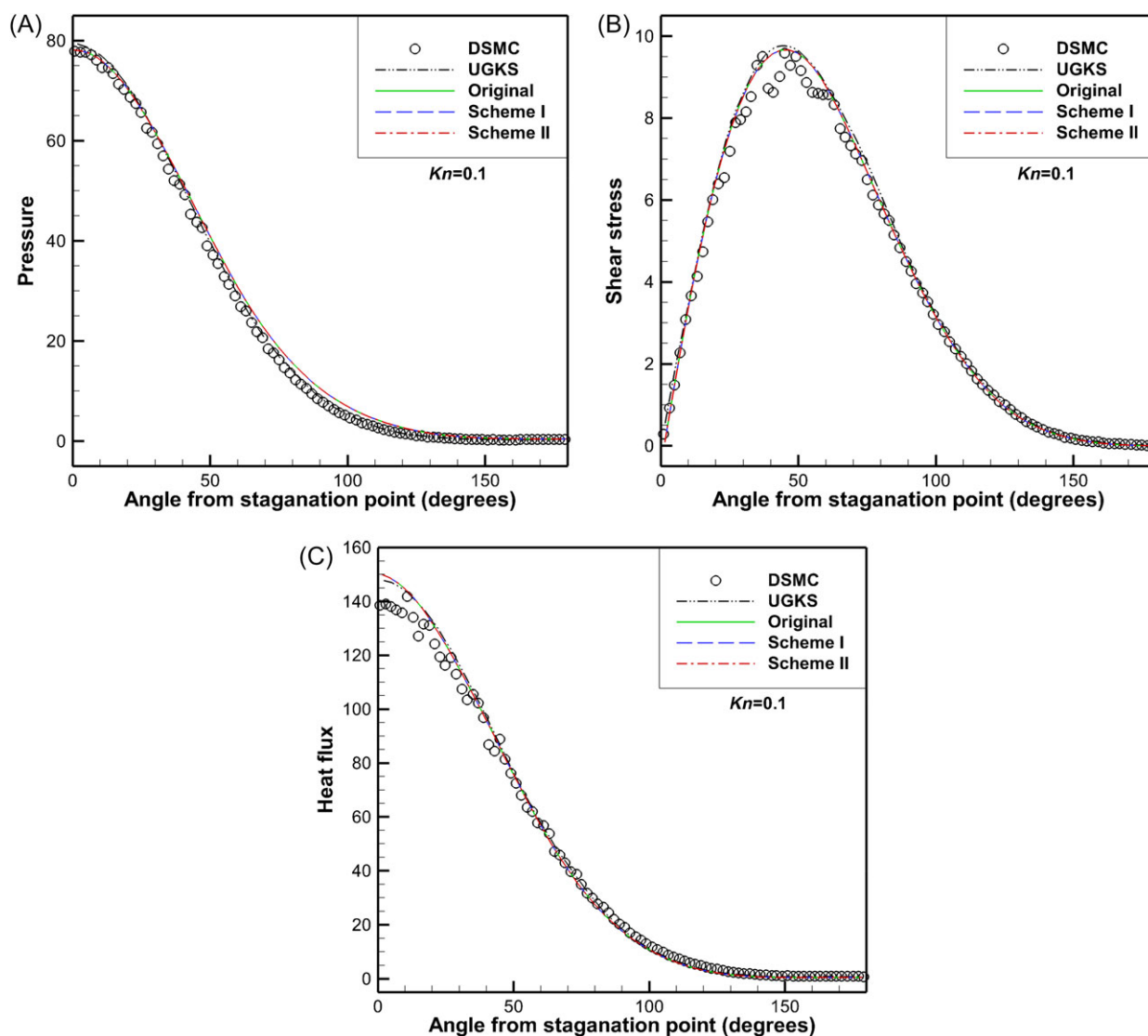


FIGURE 14 Distribution of the surface quantities along the cylinder wall from the stagnation point to the trailing edge for hypersonic flow around a cylinder at $Ma = 10$ and $Kn = 0.1$. (A) Pressure. (B) Shear stress. (C) Normal heat flux. DSMC, direct simulation Monte Carlo; UGKS, unified gas kinetic scheme [Colour figure can be viewed at wileyonlinelibrary.com]

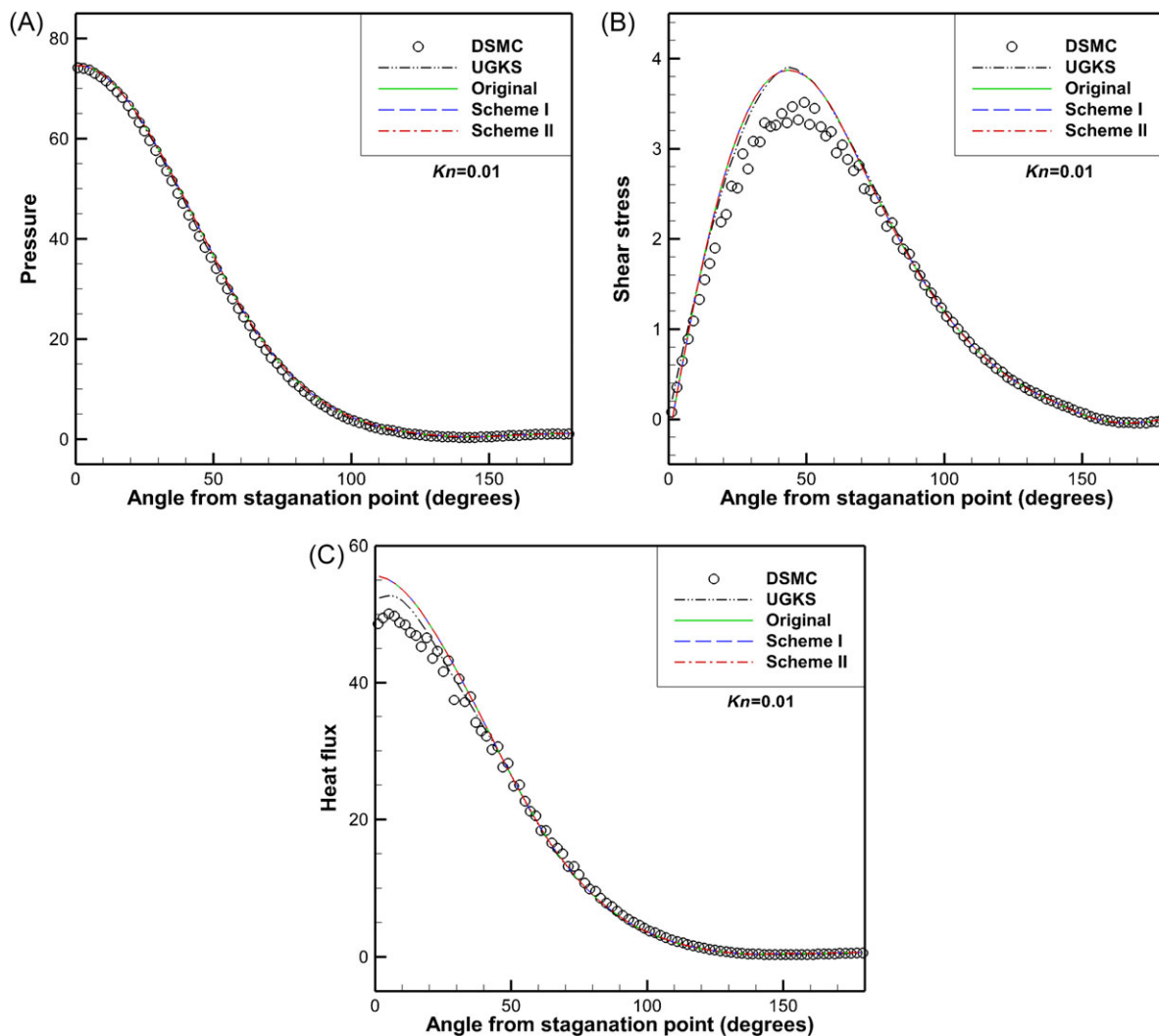


FIGURE 15 Distribution of the surface quantities along the cylinder wall from the stagnation point to the trailing edge for hypersonic flow around a cylinder at $Ma = 10$ and $Kn = 0.01$. (A) Pressure. (B) Shear stress. (C) Normal heat flux. DSMC, direct simulation Monte Carlo; UGKS, unified gas kinetic scheme [Colour figure can be viewed at wileyonlinelibrary.com]

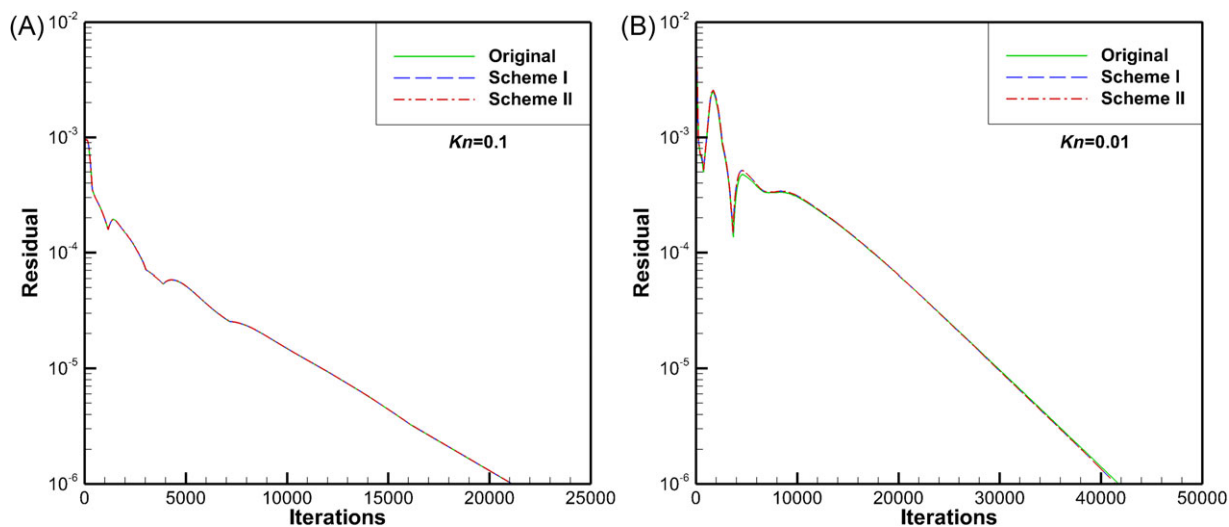


FIGURE 16 Convergence history of different methods for hypersonic flow around a cylinder at $Ma = 10$. (A) $Kn = 0.1$. (B) $Kn = 0.01$ [Colour figure can be viewed at wileyonlinelibrary.com]

TABLE 2 Computational time (hours) of different methods for hypersonic flow around a cylinder

Kn	Original	Scheme I	Scheme II
$Kn = 0.1$	104.856	149.284	137.535
$Kn = 0.01$	207.200	293.003	269.392

the results of three different methods are basically the same, and they agree well with the reference data.⁵⁹ It indicates that the solution accuracy and numerical stability of two improved schemes are consistent with the original model for simulation of hypersonic rarefied flows. In addition, the comparison of convergence history of three schemes is depicted in Figure 16 and the comparison of computational time is made in Table 2. Basically, there is no apparent difference among these three schemes in terms of convergence rate. Accordingly, the conventional DVM is more efficient than the improved schemes.

4 | CONCLUSIONS

In this work, two improved schemes for local solution reconstruction at the cell interface in DVM are presented for simulation of flows in all flow regimes. As compared with the conventional scheme, which evaluates the local solution at the cell interface by solving collisionless Boltzmann equation, the improved schemes use the local solution of Boltzmann equation with Shakhov model. To determine this local solution, the equilibrium distribution function at the cell interface has to be calculated in advance. In the first improved scheme, this equilibrium distribution function is computed by the compatibility condition, and in the second one, it is approximated by a simple average technique. The performances of two improved schemes are then compared with the conventional model by simulating several flow problems in different flow regimes.

Numerical results show that both the conventional DVM and the improved schemes can provide accurate prediction for simulation of rarefied flows, while in the continuum flow regime, the solution accuracy of two improved schemes is better than that of the conventional DVM. As far as the computational efficiency is concerned, the conventional DVM is better than the improved schemes. Specifically, the computational time of Scheme II is about 1.3-1.5 times of that of the conventional DVM. In addition, the numerical stability of three schemes is basically the same. It verifies that the approximation for equilibrium state at the cell interface by a simple average technique is reasonable and acceptable. Overall, for simulation of flows in all flow regimes, Scheme II could be the best choice among the three schemes. However, in the rarefied flow regime, the conventional DVM is preferred.

ACKNOWLEDGEMENTS

This work has been supported by the National Research Foundation Singapore, Sembcorp Industries Ltd, National University of Singapore under the Sembcorp-NUS Corporate Laboratory, Ministry of Education (MOE) of Singapore and by the National Natural Science Foundation of China (grant 11772157).

ORCID

C. Shu  <https://orcid.org/0000-0003-0825-0883>

J. Wu  <https://orcid.org/0000-0001-6963-0244>

REFERENCES

1. Broadwell JE. Study of rarefied shear flow by the discrete velocity method. *J Fluid Mech.* 1964;19(3):401-414.
2. Sharipov FM, Subbotin EA. On optimization of the discrete velocity method used in rarefied gas dynamics. *Z Angew Math Phys.* 1993;44(3):572-577.
3. Buet C. A discrete-velocity scheme for the Boltzmann operator of rarefied gas dynamics. *Transp Theory Stat Phys.* 1996;25(1):33-60.
4. Beylich AE. Solving the kinetic equation for all Knudsen numbers. *Phys Fluids.* 2000;12(2):444-465.
5. Bennoune M, Lemou M, Mieussens L. Uniformly stable numerical schemes for the Boltzmann equation preserving the compressible Navier-stokes asymptotics. *J Comput Phys.* 2008;227(8):3781-3803.

6. Aoki K, Degond P, Mieussens L. Numerical simulations of rarefied gases in curved channels: thermal creep, circulating flow, and pumping effect. *Commun Comput Phys*. 2009;6(5):919-954.
7. Chen S, Xu K, Lee C. The dynamic mechanism of a moving Crookes radiometer. *Phys Fluids*. 2012;24(11):111701
8. Yang LM, Shu C, Wu J, Wang Y. Numerical simulation of flows from free molecular regime to continuum regime by a DVM with streaming and collision processes. *J Comput Phys*. 2016;306:291-310.
9. Yang LM, Shu C, Wu J, Wang Y. Comparative study of discrete velocity method and high-order lattice Boltzmann method for simulation of rarefied flows. *Comput Fluids*. 2017;146:125-142.
10. Zhu Y, Zhong C, Xu K. Unified gas-kinetic scheme with multigrid convergence for rarefied flow study. *Phys Fluids*. 2017;29(9):096102
11. Li Z-H, Zhang H-X. Gas-kinetic numerical studies of three-dimensional complex flows on spacecraft re-entry. *J Comput Phys*. 2009;228(4):1116-1138.
12. Titarev V, Dumbser M, Utyuzhnikov S. Construction and comparison of parallel implicit kinetic solvers in three spatial dimensions. *J Comput Phys*. 2014;256:17-33.
13. Huang J-C, Xu K, Yu P. A unified gas-kinetic scheme for continuum and rarefied flows III: microflow simulations. *Commun Comput Phys*. 2013;14(5):1147-1173.
14. Yang LM, Shu C, Wu J. Numerical simulation of microflows by a DOM With streaming and collision processes. Paper presented at: ASME 2016 5th International Conference on Micro/Nanoscale Heat and Mass Transfer; 2016; Singapore.
15. Bobylev AV, Nanbu K. Theory of collision algorithms for gases and plasmas based on the Boltzmann equation and the Landau-Fokker-Planck equation. *Phys Rev E*. 2000;61:4576-4586.
16. Liu C, Xu X. A unified gas kinetic scheme for continuum and rarefied flows V: multiscale and multi-component plasma transport. *Commun Comput Phys*. 2017;22(5):1175-1223.
17. Liu F, Becker HA, Pollard A. Spatial differencing schemes of the discrete-ordinates method. *Numer Heat Transf B Fundam*. 1996;30(1):23-43.
18. Yang R, Chen G, Laroche M, Taur Y. Simulation of nanoscale multidimensional transient heat conduction problems using ballistic-diffusive equations and phonon Boltzmann equation. *J Heat Transfer*. 2005;127(3):298-306.
19. Donmez N, Graham S. A multiscale thermal modeling approach for ballistic and diffusive heat transport in two dimensional domains. *Int J Therm Sci*. 2014;76:235-244.
20. Guo Z, Xu K. Discrete unified gas kinetic scheme for multiscale heat transfer based on the phonon Boltzmann transport equation. *Int J Heat Mass Transfer*. 2016;102:944-958.
21. Mieussens L. Discrete-velocity models and numerical schemes for the Boltzmann-BGK equation in plane and axisymmetric geometries. *J Comput Phys*. 2000;162(2):429-466.
22. Li Z-H, Zhang H-X. Numerical investigation from rarefied flow to continuum by solving the Boltzmann model equation. *Int J Numer Meth Fluids*. 2003;42(4):361-382.
23. Wang P, Ho MT, Wu L, Guo Z, Zhang Y. A comparative study of discrete velocity methods for low-speed rarefied gas flows. *Comput Fluids*. 2018;161:33-46.
24. Yang JY, Huang JC. Rarefied flow computations using nonlinear model Boltzmann equations. *J Comput Phys*. 1995;120(2):323-339.
25. Kudryavtsev AN, Shershnev AA. A numerical method for simulation of microflows by solving directly kinetic equations with WENO schemes. *J Sci Comput*. 2013;57:42-73.
26. Diaz MA, Chen M-H, Yang J-Y. High-order conservative asymptotic-preserving schemes for modeling rarefied gas dynamical flows with Boltzmann-BGK equation. *Commun Comput Phys*. 2015;18(4):1012-1049.
27. Chen S, Xu K. A comparative study of an asymptotic preserving scheme and unified gas-kinetic scheme in continuum flow limit. *J Comput Phys*. 2015;288:52-65.
28. Yang LM, Shu C, Yang WM, Chen Z, Dong H. An improved discrete velocity method (DVM) for efficient simulation of flows in all flow regimes. *Phys Fluids*. 2018;30(6):062005
29. Xu K, Liu C. A paradigm for modeling and computation of gas dynamics. *Phys Fluids*. 2017;29:026101
30. Xu K, Huang J-C. A unified gas-kinetic scheme for continuum and rarefied flows. *J Comput Phys*. 2010;229(20):7747-7764.
31. Mieussens L. On the asymptotic preserving property of the unified gas kinetic scheme for the diffusion limit of linear kinetic models. *J Comput Phys*. 2013;253:138-156.
32. Xu K. *Direct Modeling for Computational Fluid Dynamics: Construction and Application of Unified Gas-Kinetic Schemes*. Singapore: World Scientific; 2015.
33. Zhu Y, Zhong C, Xu K. Implicit unified gas-kinetic scheme for steady state solutions in all flow regimes. *J Comput Phys*. 2016;315:16-38.
34. Guo Z, Xu K, Wang R. Discrete unified gas kinetic scheme for all Knudsen number flows: low-speed isothermal case. *Phys Rev E*. 2013;88:033305
35. Guo Z, Wang R, Xu K. Discrete unified gas kinetic scheme for all Knudsen number flows. II. Thermal compressible case. *Phys Rev E*. 2015;91:033313
36. Zhu L, Guo Z, Xu K. Discrete unified gas kinetic scheme on unstructured meshes. *Comput Fluids*. 2016;127:211-225.
37. Liu H, Cao Y, Chen Q, Kong M, Zheng L. A conserved discrete unified gas kinetic scheme for microchannel gas flows in all flow regimes. *Comput Fluids*. 2018;167:313-323.
38. Shakhov EM. Generalization of the Krook kinetic relaxation equation. *Fluid Dynamics*. 1968;3(5):95-96.

39. Li Z-H, Zhang H-X. Study on gas kinetic unified algorithm for flows from rarefied transition to continuum. *J Comput Phys*. 2004;193(2):708-738.
40. Van Leer B. Towards the ultimate conservative difference scheme. IV. A new approach to numerical convection. *J Comput Phys*. 1977;23(3):276-299.
41. Shu C, Wang Y, Teo CJ, Wu J. Development of lattice Boltzmann flux solver for simulation of incompressible flows. *Adv Appl Math Mech*. 2014;6(4):436-460.
42. Titarev VA. Conservative numerical methods for model kinetic equations. *Comput Fluids*. 2007;36(9):1446-1459.
43. Titarev VA. Implicit numerical method for computing three-dimensional rarefied gas flows on unstructured meshes. *Comput Math & Math Phys*. 2010;50(10):1719-1733.
44. Titarev VA. Implicit high-order method for calculating rarefied gas flow in a planar microchannel. *J Comput Phys*. 2012;231(1):109-134.
45. Wu L, Ho MT, Germanou L, et al. On the apparent permeability of porous media in rarefied gas flows. *J Fluid Mech*. 2017;822:398-417.
46. Lee CB. Possible universal transitional scenario in a flat plate boundary layer: measurement and visualization. *Phys Rev E*. 2000;62:3659.
47. John B, Gu X-J, Emerson DR. Effects of incomplete surface accommodation on non-equilibrium heat transfer in cavity flow: a parallel DSMC study. *Comput Fluids*. 2011;45(1):197-201.
48. Huang J-C, Xu K, Yu P. A unified gas-kinetic scheme for continuum and rarefied flows II: multi-dimensional cases. *Commun Comput Phys*. 2012;12(3):662-690.
49. Yang LM, Shu C, Yang WM, Wu J. An implicit scheme with memory reduction technique for steady state solutions of DVBE in all flow regimes. *Phys Fluids*. 2018;30(4):040901
50. Ghia U, Ghia KN, Shin CT. High-re solutions for incompressible flow using the Navier-stokes equations and a multigrid method. *J Comput Phys*. 1982;48(3):387-411.
51. Hou S, Zou Q, Chen S, Doolen G, Cogley AC. Simulation of cavity flow by the lattice Boltzmann method. *J Comput Phys*. 1995;118(2):329-347.
52. Lee CB, Wu JZ. Transition in wall-bounded flows. *Appl Mech Rev*. 2008;61(3):030802.
53. Yang LM, Shu C, Wu J. A simple distribution function-based gas-kinetic scheme for simulation of viscous incompressible and compressible flows. *J Comput Phys*. 2014;274:611-632.
54. Yang LM, Shu C, Yang WM, Wang Y. A simplified circular function-based gas kinetic scheme for simulation of incompressible flows. *Int J Numer Meth Fluids*. 2017;85(10):583-598.
55. Maslach GJ, Schaaf SA. Cylinder drag in the transition from continuum to free molecule flow. *Phys Fluids*. 1963;6(3):315-321.
56. Metcalf SC, Berry CJ, Davis BM. *An Investigation of the Flow About Circular Cylinders Placed Normal to a Low-Density, Supersonic Stream*. Aeronautical Research Council, Reports and Memoranda No. 3416. London, UK: Her Majesty's Stationery Office; 1965.
57. Zhu Y, Lee C, Chen X, Wu J, Chen S, Gad-el-Hak M. Newly identified principle for aerodynamic heating in hypersonic flows. *J Fluid Mech*. 2018;855:152-180.
58. Titarev VA. Application of model kinetic equations to hypersonic rarefied gas flows. *Comput Fluids*. 2018;169:62-70.
59. Yu PB. *A Unified Gas Kinetic Scheme for All Knudsen Number Flows* [PhD thesis]. Hong Kong: Hong Kong University of Science and Technology; 2013.

How to cite this article: Yang LM, Shu C, Yang WM, Wu J, Zhang MQ. Numerical investigation on performance of three solution reconstructions at cell interface in DVM simulation of flows in all Knudsen number regimes. *Int J Numer Meth Fluids*. 2019;90:545-563. <https://doi.org/10.1002/fld.4734>